Plasma Sources Science and Technology

Plasma-droplet interaction study to assess transport limitations and the role of $^{\cdot}OH$, $O^{\cdot}$, $H^{\cdot}$, $O_2(a^1\Delta_g)$, O_3, $He(2^3S)$ and $Ar(1s_5)$ in formate decomposition

To cite this article before publication: Gaurav Nayak *et al* 2021 *Plasma Sources Sci. Technol.* in press https://doi.org/10.1088/1361-6595/ac2676

Plasma-droplet interaction study to assess transport limitations and the role of $^{\cdot}$OH, O$^{\cdot}$, H$^{\cdot}$, $O_2(a^1\Delta_g)$, O_3, $He(2^3S)$ and $Ar(1s_5)$ in formate decomposition

Gaurav Nayak[1], Gaku Oinuma[2], Yuanfu Yue[1], João Santos Sousa[3] and Peter J Bruggeman[1]

[1]Department of Mechanical Engineering, University of Minnesota, Minneapolis, Minnesota 55455, USA

[2]Advanced Technology R & D Center, Mitsubishi Electric Corporation, Hyogo 661-8661, Japan

[3]Université Paris-Saclay, CNRS, Laboratoire de Physique des Gaz et des Plasmas, 91405 Orsay, France

E-mail: nayak025@umn.edu, pbruggem@umn.edu

August 2021

Abstract.

Plasmas interacting with liquid microdroplets are gaining momentum due to their ability to significantly enhance the reactivity transfer from the gas phase plasma to the liquid. This is, for example, critically important for efficiently decomposing organic pollutants in water. In this contribution, the role of $^{\cdot}$OH as well as non-$^{\cdot}$OH–driven chemistry initiated by the activation of small water microdroplets in a controlled environment by diffuse RF glow discharge in He with different gas admixtures (Ar, O_2 and humidified He) at atmospheric pressure is quantified. The effect of short-lived radicals such as O$^{\cdot}$ and H$^{\cdot}$ atoms, singlet delta oxygen ($O_2(a^1\Delta_g)$), O_3 and metastable atoms of He and Ar, besides $^{\cdot}$OH radicals, on the decomposition of formate dissolved in droplets was analyzed using detailed plasma diagnostics, droplet characterization and *ex situ* chemical analysis of the treated droplets. The formate decomposition increased with increasing droplet residence time in the plasma, with ∼70% decomposition occurring within ∼15 ms of the plasma treatment time. The formate oxidation in the droplets is shown to be limited by the gas phase $^{\cdot}$OH flux at lower H_2O concentrations with a significant enhancement in the formate decomposition at the lowest water concentration, attributed to e^-/ion–induced reactions. However, the oxidation is diffusion limited in the liquid phase at higher gaseous $^{\cdot}$OH concentrations. The formate decomposition in He/O_2 plasma was similar, although with an order of magnitude higher O$^{\cdot}$ radical density than the $^{\cdot}$OH density in the corresponding He/H_2O plasma. Using a one-dimensional reaction-diffusion model, we showed that $O_2(a^1\Delta_g)$ and O_3 did not play a significant role and the decomposition was due to O$^{\cdot}$, and possibly $^{\cdot}$OH generated in the vapor containing droplet-plasma boundary layer.

Keywords: plasma-liquid interaction, droplet, diffusion and flux limited, radicals, plasma-induced liquid phase chemistry

1. Introduction

Plasma-liquid interactions have gained significant attention in the past few years due to many promising applications, including water treatment, nanoparticle synthesis, material processing, disinfection, healthcare, food decontamination and agriculture applications [1–8]. Many of these applications rely on the transfer of reactivity from a gas phase plasma to the liquid phase. Multiphase reactive species transfer in a plasma involves several complex interactions, such as evaporation, charge transfer, and heat and mass transfer [9]. As such, the understanding of plasma-liquid interactions, including the multiphase transfer of reactivity becomes imperative, especially because of the transport limitations of highly reactive plasma-produced species.

Several plasma-liquid configurations have been developed to study and overcome transport limitations [1], however, a quantitative understanding of the reactivity transfer at the plasma-liquid interface remains elusive at large. One approach involves the plasma activation of small liquid droplets or aerosols interspersed in the gas phase plasma, which has inherent advantages compared to the interactions between plasma and a bulk liquid phase [10]. Briefly, transport of radical or ionic species produced by electron impact in the gas phase to the droplet is faster due to the small distance between the local site of production and the droplet. This rapid transport is further enhanced by the much larger surface-to-volume ratio of the micrometer-sized droplets as compared to a plasma interacting with a bulk liquid. For example, the maximum efficiency of the production of H_2O_2 with plasmas was achieved in a low power pulsed gliding arc reactor treating a spray of small water droplets [11]. Similarly, plasma-based synthesis of gold nanoparticles (AuNPs) within liquid droplets have been reported to exhibit synthesis rates several orders of magnitude higher than any other reported methods [12]. In a similar approach, substrate- and stabilizer-free metallic silver nanoparticles (AgNPs) have been synthesized during in-flight reduction of liquid droplets loaded with a $AgNO_3$ precursor [13]. Another recent work on plasma-droplet interactions reports the continuous production of NH_3 by reacting N_2 and H_2O droplets in a DBD reactor [14]. Plasma-aerosol interactions have also been studied extensively in the context of thin film deposition of organic and inorganic coatings on polymer surfaces [15–19]. In the context of decontamination, the production of reactive nitrogen species by spark discharges during electrospraying of water droplets has been reported [20]. In view of the recent COVID-19 pandemic, rapid inactivation of in-flight virus aerosols by air DBD has been reported within timescales of milliseconds, enabled by the high rate of reactivity transfer into the virus-loaded liquid micro-droplets [21–23].

Apart from the above mentioned experimental work, these unique interactions

have also been studied by modeling and simulations, e.g. the deposition of liquid droplets containing HMDSO precursor in the presence of an atmospheric pressure plasma has been studied by three-dimensional simulations [24]. A recent modeling study reported on the interaction of water micro-droplets with an air DBD using a simplified 2-D and 0-D transport model [25]. This model revealed high fluxes of reactive oxygen and nitrogen species to the droplet, leading to the accumulation and ultimately saturation of these species in the plasma-treated droplets at timescales of milliseconds. Our previous work on the determination of the reactivity transfer of $^{\cdot}$OH from the gas phase plasma to the liquid micro-droplets was likely the first measurement that showed quantitative agreement with a one-dimensional reaction-diffusion model without fitting parameters of decomposing a model hydrocarbon (formate), demonstrating the dominance of the near-interfacial reactions with $^{\cdot}$OH radicals and the limitation of the diffusion of formate in the droplet to the reactive plasma-droplet interface on the formate oxidation rate [10]. Recently, the transport of gas-phase H_2O_2 and O_3 into water micro-droplets was investigated illustrating the solvation efficiency and mass transfer of these important plasma-produced species into bulk and electrosprayed water [26].

Despite extensive research involving plasma-droplet interactions, a quantitative understanding of plasma-induced liquid phase chemistry remains in the hindsight, particularly, the chemistry of short-lived reactive species. In this work, we focus on O_2 and H_2O plasma chemistry. This allows us to focus on the dominant radicals in these plasmas, such as hydroxyl radical ($^{\cdot}$OH), atomic oxygen ($O^{\cdot}$), singlet delta oxygen ($O_2(a^1\Delta_g)$), atomic hydrogen ($H^{\cdot}$) and solvated electrons (e^-_{aq}). The effect of these species on plasma-induced liquid phase chemistry have been suggested by several research groups [6, 27–34]. The role of plasma-produced $^{\cdot}$OH radicals as the key component in initiating useful chemical reactions has been well established [1, 35, 36], although often not quantitatively. The $^{\cdot}$OH radicals have been reported to efficiently degrade many organic compounds and plays a crucial role in H_2O_2 formation [35, 37]. However, due to the limited penetration depth in the liquid [38], $^{\cdot}$OH mainly reacts at the interface and $^{\cdot}$OH-induced reactions are transport limited [39]. It is, therefore, suggested that the efficient transport of the to-be-treated compound to the plasma-liquid interface might be more critical than the flux of $^{\cdot}$OH radicals produced in the plasma itself [40, 41].

Besides $^{\cdot}$OH, the importance of $O_2(a^1\Delta_g)$ in the plasma-enabled virus inactivation has been established in O_2-containing RF plasma jets [6]. $O_2(a^1\Delta_g)$ has also been suggested to be the possible cause of selective plasma action on cancer cells [42]. The $H^{\cdot}$ radical is a major reducing species in acidic solutions [39]. The $H^{\cdot}$ radicals have been suggested to play an important role in reducing Ag^+ ions in the bulk solution into AgNPs at the interface [31]. However, $H^{\cdot}$ is strongly hydrophobic [43], and is unlikely to be transferred from the gas phase to the liquid phase [44]. Nonetheless, $H^{\cdot}$ can be produced in an acidic solution by the reaction of e^-_{aq} with H^+ ions or through

photolyses [45].

Another important plasma-generated short-lived radical species is the $O^{\cdot}$ radical with mostly unknown transport properties. Nonetheless, plasma-generated $O^{\cdot}$ atoms have been reported to diffuse into the liquid forming stable solvated $O^{\cdot}$ atoms ($O^{\cdot}_{aq}$) and react with phenol without any intermediate reactions [29]. The solvated $O^{\cdot}$ atoms have been shown to be quite efficient in phenol degradation in solution, with more than 50% of the $O^{\cdot}$ atoms leaving the He/O_2 jet nozzle entering the liquid and leading to liquid phase reactivity [28]. Similarly, OCl^- ions produced by the reaction of $O^{\cdot}$ and chloride in saline solutions have been reported to show a strong biocidal activity [46, 47]. In summary, the effect of these short-lived reactive species ($^{\cdot}OH$, $H^{\cdot}$ and $O^{\cdot}$) in driving the plasma-induced chemistry is of paramount importance and would benefit from additional quantitative experimental studies.

In the present work, we extend our previous work reported in [10] to assess the effect of $^{\cdot}OH$ species flux on transport limitations and to plasma conditions that favor other short-lived reactive species, such as $O^{\cdot}$, $H^{\cdot}$, as well as $O_2(a^1\Delta_g)$, e^-, ions and metastable atoms of He and Ar on the formate decomposition, and, thereby, establish a more detailed understanding of radical-induced liquid phase chemistry beyond $^{\cdot}OH$ radicals.

2. Methods

2.1. Experimental setup

Figure 1 depicts the schematic of the plasma-droplet reactor used in this work, the details of which can be found in [10, 48, 49]. Briefly, a capacitively-coupled diffuse RF glow plasma was generated between two parallel water-cooled electrodes separated by an inter-electrode spacing of 2 mm with an electrode cross-sectional area of 19.1×9.5 mm^2, embedded inside a PTFE housing and enclosed by quartz windows for optical access allowing droplet imaging and gas-phase spectroscopic diagnostics. The discharge was generated at atmospheric pressure in helium (ultra-pure carrier grade 99.9995%) with admixtures of O_2, H_2O and Ar as reported in table 1. For similar plasma operating conditions in helium, the measured N_2 impurity in the same reactor was around 6 ppm [48]. The total gas flow rate was varied between 0.75 and 3.0 standard liters per minute (slm), which corresponded to gas velocities in the range of 0.5 and 2.1 m s^{-1} at the center of the inter-electrode gap. The gas residence time (t_{res}) in the discharge gap varied between 7 and 29 ms.

The discharge power in different gas admixtures was calculated as described in [10, 50], and reported in table 1. The reported images of plasmas in different gas mixtures were taken using a digital camera (Nikon D3100) with a micro-focus lens (Nikon Micro-Nikkor 105 mm) at a fixed exposure of 1 s.

The reactor also includes an on-demand micro-droplet dispenser and a droplet collector mounted on the top and bottom of the PTFE housing, respectively. The

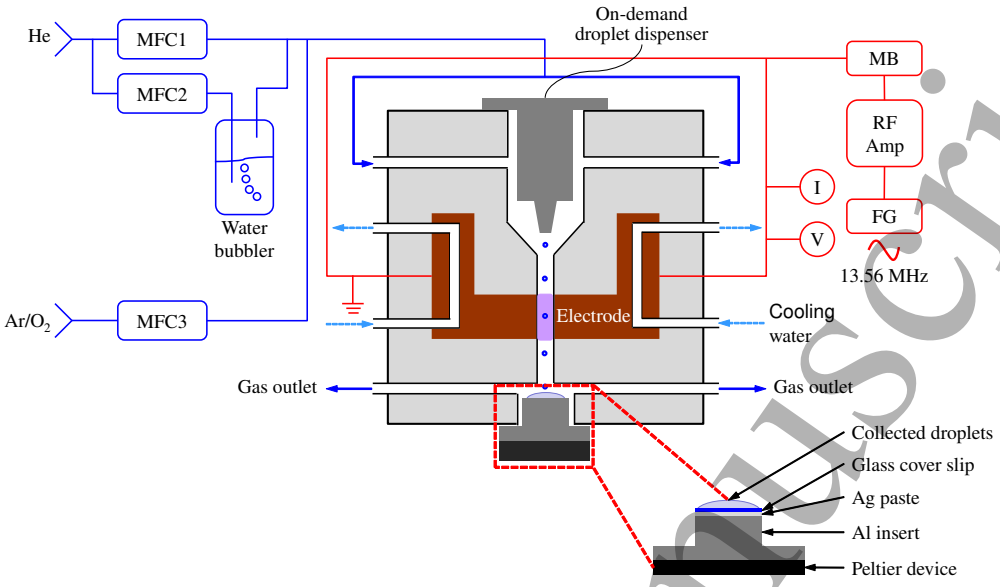

Figure 1. Schematic of the RF-driven plasma reactor with on-demand droplet dispenser. FG, function generator; RF Amp, RF amplifier; MB, matching box; MFC, mass flow controller; I, current probe; V, voltage probe.

Table 1. Operating plasma conditions used in this work.

Gas	Power (W)
He + 0.2% O_2	14.2 ± 0.6
He + 0.2% H_2O	14.3 ± 0.4
He + 17% Ar + 0.2% H_2O	13.4 ± 0.5

droplet dispenser (MicroFab Technologies Inc. MJ-ATP-01-070) with a 70 μm (ϕ) orifice was used to generate droplets of 41 ± 2 μm in diameter at a frequency of 1600 Hz actuated by an external controller (MicroFab Technologies Inc. JetDrive™ III CT-M5-01). The ejected droplets were carried with a downward flowing feed gas through the inter-electrode plasma gap before reaching the droplet collector, the surface of which was cooled to sub-zero temperatures to freeze the plasma-treated droplets upon impact. The detailed schematic of the droplet collector is also shown in figure 1 and further related information can be found in [10]. The plasma-droplet reactor was mounted on a micrometer-controlled translational stage allowing for spatially resolved diagnostics along the gas flow direction as well as across the inter-electrode gap.

2.2. Droplet imaging and residence time

The droplet motion was captured by microscopic imaging using a fast-framing camera (Photron FASTCAM Mini UX50) mounted with a micro-focus lens L2 (Nikon Micro-

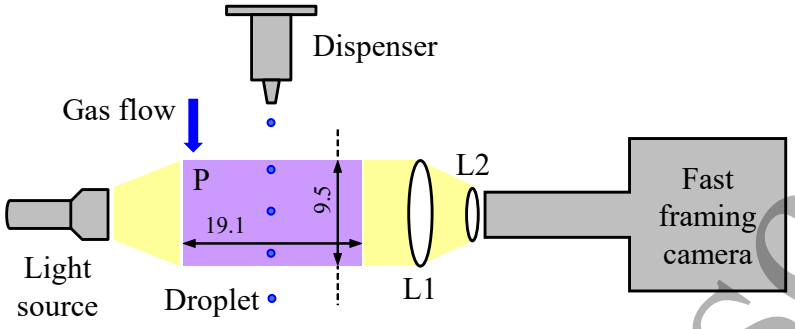

Figure 2. Experimental setup to determine the residence time of droplets in the plasma using fast frame imaging: P, plasma; L1, focusing lens; L2, adjustable lens. The provided dimensions have mm units.

Nikkor 105 mm) and an extension tube to achieve a high magnification and an image resolution of 1.7 μm/px as shown in figure 2. The path of the droplets was illuminated with an LED flash light and the images were detected by the fast-framing camera via a convex lens L1. The camera settings, i.e. frame rate of 16000 frames per second and shutter speed of 7.8 μs, along with the intensity and position of the flash light were fixed throughout the work. The droplet recordings were analyzed using the image processing software ImageJ [51]. The details of the analysis approach used can be found in [10]. The residence time of droplets in the plasma was determined from the droplet position and the local droplet velocity by recording the droplet motion along its trajectory.

2.3. Liquid-phase analysis

We used sodium formate as the model organic compound because of its simple molecular structure and known chemistry with various radical species in water in the context of photolysis [45]. This compound has been successfully used to elucidate OH-induced oxidation in droplets in plasmas [10]. A 2 mM formate solution was prepared by mixing equimolar amounts of formic acid and sodium hydroxide in HPLC-grade deionized water to achieve a pH of $\sim$ 7.5. For the *ex situ* decomposition measurements, droplets containing 2 mM formate were dispensed and carried though the plasma by the gas flow at different gas flow rates (0.75 to 3.0 slm) to change the droplet residence times in the plasma. At a droplet dispensing frequency of 1600 Hz, there are up to 20 droplets within the plasma region at any given moment for the smallest gas flow rate of 0.75 slm, which might impact the plasma composition in the bulk [10]. However, the effect of the change in the $^{\cdot}$OH radical density on the formate decomposition due to the increase in the local water vapor concentration has been estimated to be <10% [10].

There are mainly two reasons for selecting a high droplet dispensing frequency: (a) the sampling time is significantly reduced, leading to less evaporation of the collected droplets (an ice layer is formed after freezing of a large amount of droplets, which acts as a layer of insulation and avoids further freezing of additional droplets on impact), and (b) a lower droplet frequency (400 Hz) leads to larger variability in the absorption measurements due to increased variability in solution recovery at the bottom of the reactor. At lower frequency, the sampling time increases, which leads to changes in the surface properties of the glass cover slip from hydrophobic to hydrophilic by the plasma. The droplets were sampled for 2.5–3 min, which allowed a collection of 10 μl sample solution for further chemical analysis. Using the assay as detailed in [10], the formate concentration in the droplets was quantified by optical absorption spectroscopy (OAS). All measurements were performed in triplicates and the reported error bars represent the standard deviation of these 3 measurements.

2.4. Plasma characterization

2.4.1. Hydroxyl radical ($^{\cdot}$OH) *density* The absolute number density of $^{\cdot}$OH (n_{OH}) and gas temperature (T_{g}) in He/Ar/H_2O plasma was determined by employing broadband absorption spectroscopy (BAS) in the UV region as described in detail in [52–54]. The measurement of the rotational temperature of the ground state OH(X) molecule in He/H_2O and He/Ar/H_2O plasmas was previously shown to be a good representation of the gas temperature [52, 55, 56]. The absolute density and T_{g} were determined by fitting the experimentally recorded absorption spectrum with a synthetic spectrum based on the least-square method of the Curve Fitting Toolbox in MATLAB as described in [53]. The reported uncertainty represents the 95% confidence intervals of the fitting. These measurements were performed at different axial locations in the center of the discharge gap.

2.4.2. Atomic hydrogen ($H^{\cdot}$) *density* The absolute density of atomic $H^{\cdot}$ in He/H_2O and He/Ar/H_2O plasmas was measured by two photon absorption laser induced fluorescence (TaLIF) exciting the H($1s^2S_{\frac{1}{2}} \rightarrow 3d^2D_{\frac{3}{2},\frac{5}{2}}$) transition at 205.08 nm with a corresponding H_α($3d^2D_{\frac{3}{2},\frac{5}{2}} \rightarrow 2p^2P_{\frac{1}{2},\frac{3}{2}}$) fluorescence transition at 656 nm [57, 58]. The experimental configuration for TaLIF is described in [59, 60], which included a nanosecond pulsed Nd:YAG laser (Spectra-Physics Lab-170-10H, FWHM = 8 ns) operating at 532 nm that was used to pump a dye laser (Sirah Precision Scan). The resulting UV laser beam at 205 nm was focused by a plano-convex lens (f = 25 cm) into the plasma through an optical access provided by a quartz window mounted at the bottom of the reactor and the beam traversed through the length of the discharge gap (9.5 mm) as shown schematically in figure 3. The resulting fluorescence at 656.28 nm normal to the direction of the laser beam was recorded through a band pass filter (Lattice Electro Optics 656-F10-10) placed in front of an iCCD camera (Andor iStar

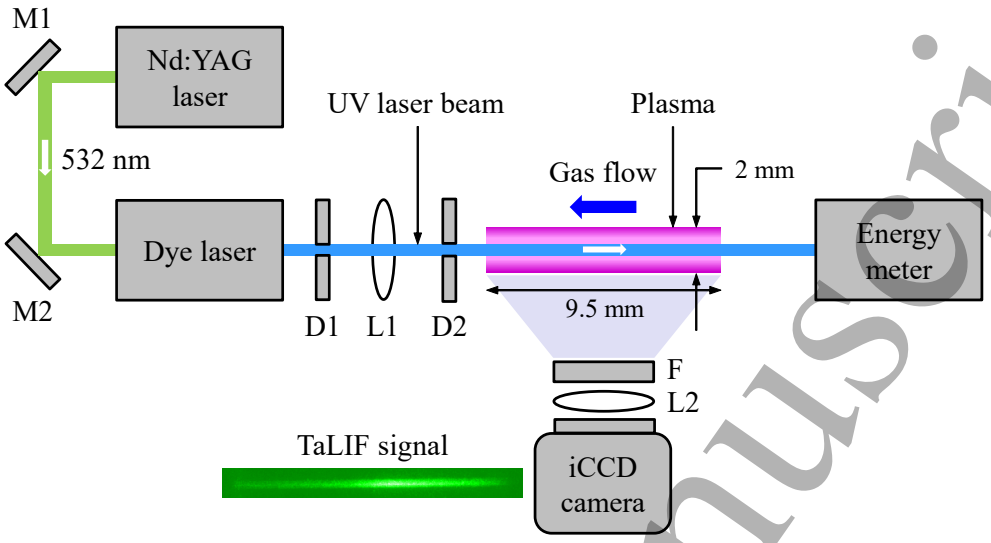

Figure 3. Schematic of the TaLIF setup used in this work for H density measurement: M1 and M2, 532 nm high reflector mirrors; D1 and D2, diaphragms; L1, quartz focusing lens; F, 656 nm optical band pass filter; L2, UV lens. See text for details.

340) mounted with a UV lens (Nikon 105 mm F4.5 UV). The absolute calibration of the H· density was achieved by measuring the TaLIF signal of a known concentration of Kr mixed with Ar feed gas at a total flow rate of 1.5 slm in the same setup and by using the following transition Kr($4p^6\ {}^1S_0 \rightarrow 5p'[3/2]_2$) at 204.13 nm with corresponding fluorescence transition Kr($5p'[3/2]_2 \rightarrow 5s[3/2]_1$) at 587.1 nm. Details of the calibration procedure can be found in [58–60]. During the TaLIF measurements, no droplets were dispensed in the plasma reactor.

2.4.3. Ar metastable ($1s_5$) *density* The absolute densities of atoms in the metastable state of argon ($1s$) in He/Ar/H_2O plasma were measured using BAS. The optical setup for the spectrally resolved measurements is identical as described in [49]. The time-averaged densities were measured across the plasma gap with a spatial resolution of 40 μm without dispensing the droplets.

2.4.4. Singlet delta oxygen ($O_2(a^1\Delta_g)$) *and ozone* (O_3) *densities* The gas-phase density of $O_2(a^1\Delta_g)$ in the plasma effluent was measured by infrared optical emission spectroscopy (IR OES). The details of the measurement technique are reported in [61]. The experimental setup used in this study is similar to the one described in [62], with a $O_2(a^1\Delta_g)$ density detection limit of 4×10^{13} cm^{-3}. The actual $O_2(a^1\Delta_g)$ density in the plasma volume ($n_{O_2(a^1\Delta_g)}(t = 0)$) was determined from the measured $O_2(a^1\Delta_g)$

density in the effluent ($n_{O_2(a^1\Delta_g)}(t_{res})$) by considering the gas residence time (t_{res}) and the effective lifetime of $O_2(a^1\Delta_g)$ (τ_{eff}) in the effluent by the following equation [62]:

$$\frac{n_{O_2(a^1\Delta_g)}(t_{res})}{n_{O_2(a^1\Delta_g)}(t=0)} = \exp\left(-\frac{t_{res}}{\tau_{eff}}\right), \quad (1)$$

where τ_{eff} was determined by the collisional quenching of $O_2(a^1\Delta_g)$ in the discharge effluent dominated by O_2 and O_3. The O_3 density in the effluent of the plasma was measured by OAS at 253.7 nm using the Beer-Lambert law as described in [62].

2.4.5. Electron density and temperature from continuum emission In weakly ionized plasmas, such as the atmospheric pressure glow discharges reported in this work, with a low degree of ionization (typically $< 10^{-4}$), the continuum radiation originating from the interactions between free electrons and neutral atoms or the neutral bremsstrahlung is dominant [63]. By fitting the absolute intensity of the recorded plasma continuum emission with the theoretical neutral bremsstrahlung spectrum, the electron density (n_e) and temperature (T_e) can be determined [64]. Briefly, the time and spatially averaged absolute plasma emission was recorded by optical emission spectroscopy and the absolute calibration was performed using a calibrated tungsten halogen lamp. The absolute spectral irradiance of the plasma, $I_P(\lambda)$ relates to the emissivity, ϵ as follows:

$$\epsilon = I_P(\lambda) \times \frac{d^2}{V_P}, \quad (2)$$

where d and V_P are the calibration distance and the plasma volume, respectively. The details of the measurement technique and data analysis can be found in [49]. For the electron-atom bremsstrahlung cross-section of gas mixtures (σ_{ea}^B), the elastic electron-atom momentum transfer cross-sections were obtained from the Phelps database for He, Ar and O_2 [65–67], and the Itikawa and Hayashi databases for H_2O [68–71]. The weighted average of the momentum transfer cross-sections of the gas mixtures were used for the calculation of the bremsstrahlung cross-section. Similarly, the non-Maxwellian EEDF of the corresponding gas-mixtures were determined from Bolsig+ [65, 68, 69, 72]. When using a Maxwellian EEDF, T_e is smaller up to 35% and n_e is larger up to 112%. A more detailed description on the effect of the EEDF on T_e and n_e determination can be found in [49]. For plasmas containing H_2O, the H_2 continuum also significantly contributes to the emission spectrum besides the neutral bremsstrahlung radiation [63]. The H_2 continuum radiation fitting is performed by following the procedure described in [63]. The measured absolute emission spectrum is fitted by the combination of two emissivities (ϵ_{total}), the electron-neutral bremsstrahlung (ϵ_{ea}) and the H_2 continuum (ϵ_{H_2}). The uncertainty in the determination of T_e and n_e is attributed to the uncertainty in the fit and random

variation in the absolute intensity of the plasmas as well as the uncertainty in the absolute calibration of the calibrated lamp emissions.

2.5. 1D reaction-diffusion model

Diffusion is the dominant transport mechanism of reactive species in the droplet for plasma treatment times up to 15 ms. Hence, a 1D reaction-diffusion model, reported by Oinuma *et al.* [10], was used to evaluate the plasma-induced oxidation of formate in the droplet. A summary of the model is presented here. The model assumes a homogeneous plasma with a near droplet boundary layer allowing only radial transport of species into the droplet with a diffusion profile, and also assumes that there are no reactions in the gas phase (see further). The time and spatial evolution of an aqueous species was governed by the 1D reaction-diffusion equation in spherical coordinates:

$$\frac{\partial A_j}{\partial t} = D_{\mathrm{l},j}\left(\frac{2}{r}\frac{\partial A_j}{\partial r} + \frac{\partial^2 A_j}{\partial r^2}\right) + \Sigma_i k_{ij} A_i A_j, \tag{3}$$

with A_j the aqueous concentration of the species j, $D_{\mathrm{l},j}$ the aqueous diffusion coefficient of species j in the droplet, r the radial position in the droplet, and $\Sigma_i k_{ij} A_i A_j$ the sum of all the reaction rates involving species j with reaction rate coefficient $k_{i,j}$. Equation (3) was solved numerically with two boundary conditions. The symmetric boundary condition at the center of the droplet is given by:

$$D_{\mathrm{l}}\left(\frac{\partial A}{\partial r}\right)_{r=0} = 0, \tag{4}$$

and the plasma-droplet interface boundary condition is given by the mass continuity of species at the droplet interface taken from [73]

$$D_{\mathrm{g}}\left(\frac{\partial G}{\partial r}\right)_{r=R_{\mathrm{p}}} = \frac{1}{4}\alpha v_{\mathrm{th}}\left[G\left(R_{\mathrm{p}},t\right) - \frac{A\left(R_{\mathrm{p}},t\right)}{H'}\right], \tag{5}$$

with G the gas-phase density of species, D_{g} the gas-phase diffusion coefficient, R_{p} the droplet radius, α the mass accommodation coefficient, v_{th} the mean speed of the molecule in the gas and H' the dimensionless Henry's law constant. For a detailed discussion on the 1D diffusion-reaction model and the adopted reaction mechanism, the reader is referred to [10].

The following additional assumptions were made using this model:

- the droplet experiences a negligible reduction in its diameter (see further);
- the liquid temperature remains close to 300 K [10];
- the effect of convection on the formate decomposition inside the droplet is negligible [10]; and
- the diffusion time of gas phase radicals through the droplet boundary is smaller than the radical lifetime [10].

In the case of He/H_2O plasma, the model was simulated for α, H' and k_{OH} (the rate coefficient of the reaction of $^{\cdot}OH$ with formate) values of 0.83, 662 and 3.2×10^9 $M^{-1}s^{-1}$, respectively, and measured gas-phase $^{\cdot}OH$ densities for corresponding H_2O concentrations. The H_2O_2 concentration input for the model was obtained from [10].

3. Results and discussions

3.1. Plasma characterization

3.1.1. Emission It is well established that formate does not readily react with long-lived species such as H_2O_2 and O_3 [74], hence, short-lived radicals are required for formate decomposition. We used He/H_2O, He/O_2 and $He/Ar/H_2O$ to generate plasmas to assess the effect of different reactive species ($O^{\cdot}$, $O_2(a^1\Delta_g)$, $H^{\cdot}$, $^{\cdot}OH$, He_m and Ar_m) on the decomposition of formate. The plasmas were operated at an RF power of ~14 W (table 1). The images of plasmas in the different gas mixtures with the operating conditions reported in table 1 are shown in figure 4. The He/O_2 plasma has whitish glow near the sheath edge while the He/H_2O and $He/Ar/H_2O$ cases are more bluish/purple in color. In all cases, the emission at the sheath edges is the strongest, while the intensity drops in the bulk of the discharge, with a maximum drop of ~ 50% in the case of He/O_2 and a minimum of ~ 30% in the case of $He/Ar/H_2O$ plasmas. In the case of the $He/Ar/H_2O$ plasma operating at 13.4 W, the visible plasma does not fill the entire inter-electrode gap as shown in figure 4(c). In the $He/Ar/H_2O$ plasma, emission starts to fade from the top part of the electrode and grows at the bottom part in the direction of the gas flow. This phenomenon becomes more prominent with increasing gas flow rates (not shown). This could be due to the build up of species, such

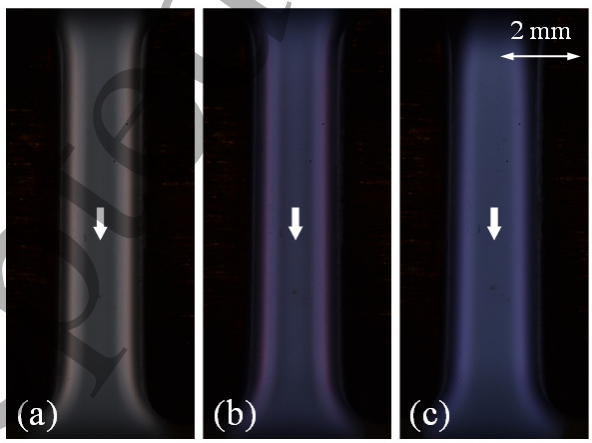

Figure 4. Digital color images of the plasma operated in (a) He + 0.2% O_2, (b) He + 0.2% H_2O, and (c) He + 17% Ar + 0.2% H_2O, at a total gas flow rate of 1.5 slm. The white arrows represent the direction of the gas flow.

as electrons, ions and metastable atoms, to reach steady state. The flow transports these species downstream enhancing the plasma emission at the bottom edge of the electrode compared to the plasma at the upper edge of the electrode. The He/Ar/H_2O plasma emission seems to even extend significantly beyond the metal electrode region. This could be due to the afterglow emission as reported in [75].

3.1.2. Gas temperature Figure 5 shows the variation in the gas temperature along the axial direction of the plasma in He/H_2O [10] and He/Ar/H_2O plasmas at a total gas flow rate of 1 slm as measured by $^{\cdot}OH$ absorption spectroscopy. The gas temperature increases along the direction of the gas flow to a steady-state temperature of 350 K and 450 K in the He/H_2O and He/Ar/H_2O plasmas, respectively. However, the gas temperature in the He/Ar/H_2O plasma attains a steady-state at a larger distance from the upper end of the electrode (∼5 mm), consistent with the smaller plasma size and larger steady-state gas temperature. The higher gas temperature for the He/Ar/H_2O compared to the He/H_2O plasma is further enhanced by the reduction in thermal conductivity of the gas mixture as Ar has a thermal conductivity that is almost an order of magnitude lower than that of helium [76]. Furthermore, at a higher gas flow rate of 5 slm, the maximum gas temperature in He/Ar/H_2O plasma drops to 350 K. Due to the similar concentration of O_2 in He/O_2 plasma (0.2%) to that of H_2O in the He/H_2O plasma, the gas temperature in He/O_2 plasma is expected to be

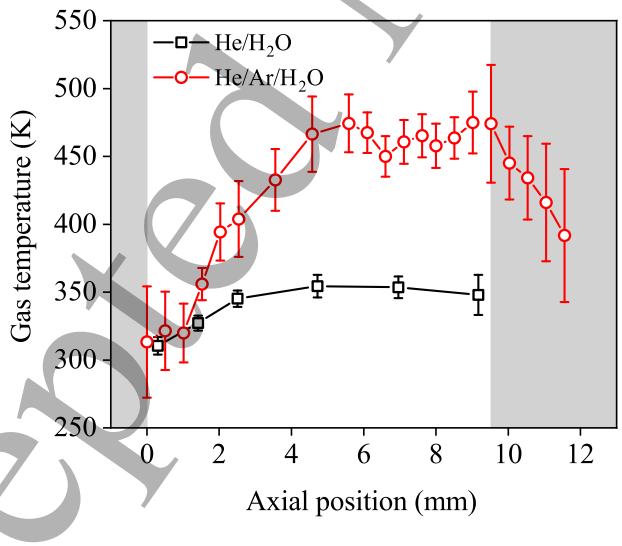

Figure 5. Spatial distribution of the gas temperature in the axial direction of He + 0.2% H_2O and He + 17% Ar + 0.2% H_2O plasmas at a gas flow rate of 1.0 slm. The white region represents the electrode zone in the axial direction. The data for He + 0.2% H_2O plasma is taken from [10].

similar to that in the He/H_2O plasma. The maximum increase in the gas temperatures assuming that all heat is removed through forced convection by the gas flow rate of 1 slm are $\sim$ 990 K and $\sim$ 440 K for He/H_2O and $He/Ar/H_2O$ plasmas, respectively. The measured gas temperatures do not exceed 500 K suggesting that a significant amount of the energy deposited by the plasma is removed through the (water-cooled) electrodes.

3.1.3. Electron temperature and density The electron properties in the investigated plasmas were determined from the emissivity measurements of the continuum radiation as described in Section 2.4.5. The results of the emissivity fitting with the experimentally obtained absolute intensity of the continuum radiation are shown in figure 6.

The emissivity in the He/O_2 (figure 6(a)) plasma could not be fitted completely in the near-UV region, which might be due to the significant contribution of molecular emission by nitrogen impurities and $^{\cdot}OH$ radicals. In our previous work, an electron density of $\sim 10^{19}$ m^{-3} was determined in Ar plasma (13.5 W) [49]. However, in this study, in a mixture of $He/Ar/H_2O$ plasma, n_e was estimated to be around 1.5×10^{17} m^{-3}, which is more similar to a helium plasma [49]. This is consistent with the dilution of Ar with 83% helium and the presence of H_2O vapor, an electronegative gas. For H_2O containing plasmas, apart from bremsstrahlung radiation, the H_2 continuum is also considered. The H_2 continuum radiation fitting for He/H_2O and $He/Ar/H_2O$ plasmas are shown in figure 6(b) and (c). In He/H_2O plasma, due to the electronegative nature, T_e is expected to rise with a reduction in n_e [77] as compared to He plasma [49], which is consistent with the result shown in figure 6(b). As expected, the He/H_2O and He/O_2 plasmas have very similar n_e and T_e (figure 6(a)).

The electron density in all the investigated plasmas varies at most by a factor 2 and is of the order of $\sim 10^{17}$ m^{-3}. However, a larger variation in T_e is observed from 3.1 eV in $He/Ar/H_2O$ to 3.8 eV in He/H_2O plasma. Based on the accuracy of the fit and the random variation in repeated measurements of the emission intensities of the lamp and the plasma, an uncertainty of 11% in T_e and 28% in n_e is estimated. The uncertainty in n_e due to the addition of H_2 continuum to the overall fit does not necessarily increase, however, it impacts the uncertainty in T_e more significantly. The electron properties (n_e and T_e) determined from the continuum emission were compared with power balance estimates previously [49], and while for helium, a good agreement was obtained, in the case of argon, significant discrepancies were found which might suggest that the n_e and T_e determined for the $He/Ar/H_2O$ mixture might be less accurate and further validation of the continuum emission approach might be beneficial.

3.1.4. He/Ar metastable species The metastable atoms produced in RF plasmas are important sources of energy sinks and might influence the chemistry in the plasma-

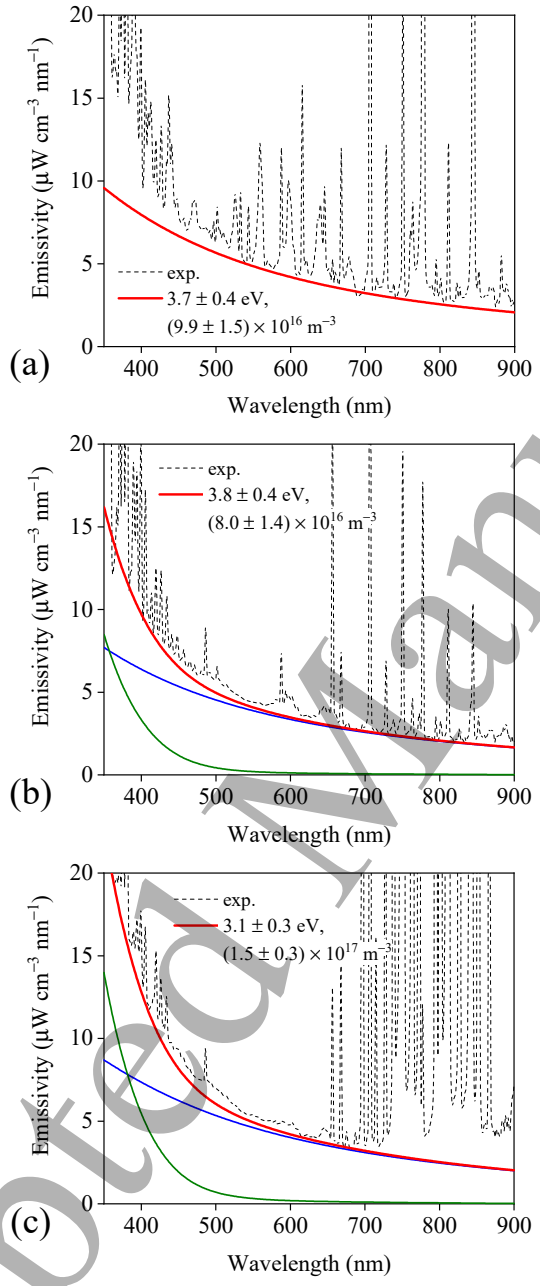

Figure 6. The measured absolute intensity of plasma emission in (a) He + 0.2% O_2, (b) He + 0.2% H_2O, and (c) He + 17% Ar + 0.2% H_2O plasmas at a total gas flow rate of 1 slm fitted with the calculated emissivities of the electron-atom bremsstrahlung continuum radiation using a non-Maxwellian EEDF. The corresponding n_e and T_e are also shown. The blue, green and red solid curves in (b) and (c) represent ϵ_{ea}, ϵ_{H_2} and ϵ_{total}, respectively.

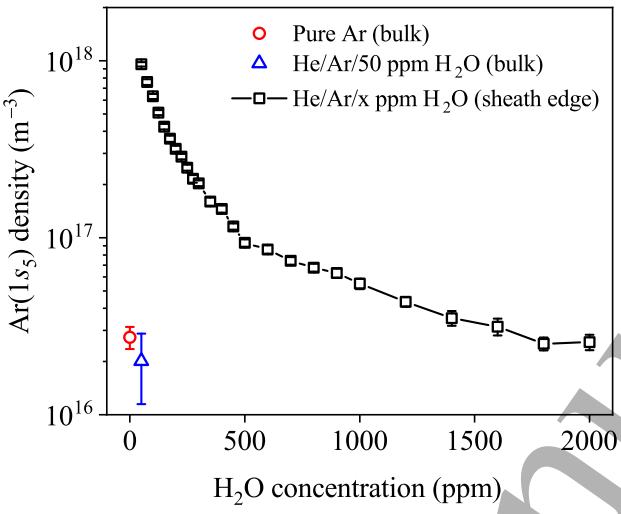

Figure 7. Time-averaged absolute densities of Ar($1s_5$) metastable atoms in He + 17% Ar + x ppm H_2O plasma as a function of H_2O concentration at a total gas flow rate of 5 slm. The power varied from 14.3 W to 13.4 W corresponding to 50 ppm and 2000 ppm H_2O, respectively. The measurements were taken at the position of the maximum density of Ar($1s_5$) atoms near the sheath edge. The densities of Ar($1s_5$) metastable atoms in the bulk of the discharge in pure Ar and He + 17% Ar + 50 ppm H_2O plasmas are also shown.

treated droplet. We investigated the effect of varying H_2O concentration from 50 to 2000 ppm (i.e. 0.05–0.2%) in He/Ar/H_2O plasma on the Ar($1s_5$) metastable densities. The corresponding densities near the sheath edge are shown in figure 7. The maximum density of Ar($1s_5$) metastable atoms in He + 17% Ar + 0.2% H_2O near the sheath region is $\sim 2.6 \times 10^{16}$ m^{-3}, while the density in the bulk of the plasma, where the droplets are mostly located during in-flight treatment, is below the detection limit of the measurement ($\sim 1.0 \times 10^{16}$ m^{-3}). The ratio of the densities of Ar($1s_5$) metastable atoms in the sheath to the bulk is ~30 in pure Ar plasma [49], and ~55 in He/Ar plasma with low H_2O concentration (50 ppm). However, to assess the possible role of these metastable atoms in reactions in the droplets, a detailed flux analysis is necessary. The effective lifetime of Ar($1s_5$) metastable atom in the presence of 0.2% H_2O is estimated to be ~45 ns, which is more than 4 orders of magnitude faster than its diffusion time (~1 ms). Hence, only local production of Ar($1s_5$) at the plasma-droplet interface can lead to liquid phase reactions. The total flux of electrons (Γ_e) and Ar($1s_5$) ($\Gamma_{Ar(1s_5)}$) to a droplet of diameter 41 μm can be estimated by the following equations [10]:

$$\Gamma_e \approx \frac{1}{4} n_e \overline{v}_e \times 4\pi R_p^2 \exp\left(\frac{q\phi}{kT_e}\right), \text{ and} \quad (6)$$

$$\Gamma_{\mathrm{Ar}(1s_5)} \approx \frac{1}{4}\alpha G_{\mathrm{Ar}(1s_5)} v_{\mathrm{th}} \times 4\pi R_{\mathrm{p}}^2, \tag{7}$$

where $\overline{v}_{\mathrm{e}}$, $q\phi$, kT_{e} and $G_{\mathrm{Ar}(1s_5)}$ are the mean speed of electrons, the droplet potential, the electron temperature and the gas-phase bulk density of $\mathrm{Ar}(1s_5)$ atoms, respectively. The droplet potential as estimated from a kinetic electron model involving interaction of a non-emitting spherical body (droplet, in this case) with a continuum-plasma solution was roughly around $4 \times kT_{\mathrm{e}}$ [78]. Considering n_{e} and T_{e} in the bulk of the $\mathrm{He/Ar/H_2O}$ plasma estimated from the continuum radiation measurement (see figure 6(c)) and a droplet potential $q\phi \approx 4 \times kT_{\mathrm{e}}$, an electron flux of 4.3×10^{12} $\mathrm{s^{-1}}$ is estimated. Assuming an α of 1 and $G_{\mathrm{Ar}(1s_5)}$ corresponding to the detection limit of the measurement, the maximum $\mathrm{Ar}(1s_5)$ flux to the droplet is estimated to be 5.3×10^9 $\mathrm{s^{-1}}$, which is almost 3 orders of magnitude smaller than the electron flux. As the $\mathrm{Ar}(1s_5)$ density will be significantly depleted at the droplet interface compared to the bulk plasma and the lifetime is too small for significant transport, $\mathrm{Ar}(1s_5)$ metastable atoms do not play a dominant role in the droplet chemistry.

The dominant metastable atom in helium ($\mathrm{He}(2^3S)$) has been previously investigated in He with 50 ppm $\mathrm{H_2O}$ plasma and the densities were below the detection limit (3.4×10^{17} $\mathrm{m^{-3}}$) [48], which suggests that the $\mathrm{He}(2^3S)$ density would be even smaller in the presence of 0.2% $\mathrm{H_2O}$. Using a similar approach as for $\mathrm{Ar}(1s_5)$, the maximum total $\mathrm{He}(2^3S)$ flux to the droplet is estimated to be ~7.5 times smaller than that of the electron flux. Similar conclusions can be made for $\mathrm{He/O_2}$. Hence, the effect of He metastable atoms on the droplet chemistry is also negligible for all plasma conditions. To summarize, the effect of the atomic He/Ar metastable species on plasma-induced chemistry in the droplet is dominated by $\mathrm{e^-}$/ion flux to the droplet.

3.1.5. Radicals One of the dominant reactive species in water containing plasmas is the ˙OH radical. To investigate the role of ˙OH radicals, the gas-phase ˙OH densities in $\mathrm{He/H_2O}$ [10] and $\mathrm{He/Ar/H_2O}$ plasmas were measured without the presence of droplets using broadband absorption spectroscopy as discussed in Section 2.4.1. Figure 8(a) shows the axial variation of the ˙OH densities in $\mathrm{He/H_2O}$ and $\mathrm{He/Ar/H_2O}$ plasmas at a total gas flow rate of 1 slm. The ˙OH radical densities in the $\mathrm{He/Ar/H_2O}$ plasma are almost twice those in the $\mathrm{He/H_2O}$ plasma.

In both plasmas, the ˙OH density increases along the direction of the gas flow, attains a steady-state density in the center of the discharge, and decays rapidly at the bottom edge of the electrode in the afterglow. The major ˙OH production mechanism in $\mathrm{He/H_2O}$ plasma is via electron-impact dissociation of water (R1), which contributes to almost 50% of the total ˙OH generation in a parallel plate capacitively coupled RF discharge operating at similar conditions as studied in this work [79], while the dominant loss mechanism is through two-body recombination with ˙OH radicals to

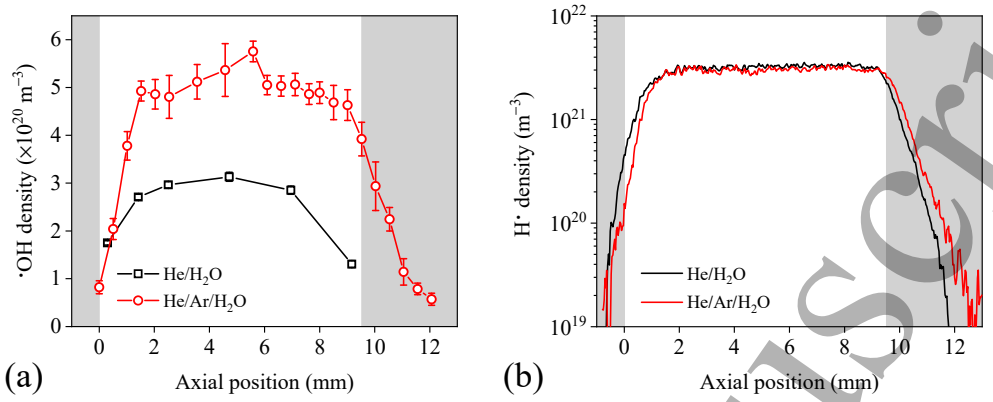

Figure 8. Absolute number densities of (a) ·OH radicals, and (b) H· radicals measured as a function of the axial position in the bulk of He + 0.2% H_2O and He + 17% Ar + 0.2% H_2O plasmas at a gas flow rate of 1.0 slm. The data for ·OH density in He + 0.2% H_2O plasma in (a) is taken from [10]. The white region represents the location of the electrodes in the axial direction.

produce H_2O (R2) in addition to recombination reactions (R3) and (R4) that lead to the formation of H_2O_2 and H_2O, respectively, as shown below.

$$e^- + H_2O \rightarrow H + OH + e^- \quad \text{(R1)}$$

$$OH + OH \rightarrow H_2O + O \quad \text{(R2)}$$

$$OH + OH + M \rightarrow H_2O_2 + M \quad \text{(R3)}$$

$$OH + H + M \rightarrow H_2O + M \quad \text{(R4)}$$

Here, M = Ar or He. The lifetime of ·OH in He/H_2O plasma can be estimated as

$$\tau_{\text{lifetime}} = \left[2k_{(R2)}n_{OH} + 2k_{(R3)}n_{OH}n_{He} + k_{(R4)}n_{He}n_{H} + \frac{D_{OH}}{\Lambda^2}\right]^{-1}, \quad (8)$$

where k_i is the reaction rate coefficient of reaction R_i [80], D_{OH} the diffusion coefficient of $^{\cdot}OH$ in He gas at a gas temperature of 350 K [81], and $\Lambda = L/\pi$, with L being half of the discharge gap. The absolute $H^{\cdot}$ density (n_H) is obtained from the measured TaLIF (see further). The $^{\cdot}OH$ lifetime in He/H_2O plasma from (8) is estimated to be ~73 μs. However, in $He/Ar/H_2O$ plasma, the $^{\cdot}OH$ lifetime is estimated to be ~114 μs, even though the $^{\cdot}OH$ density is larger than in He/H_2O plasma. This is due to the higher gas temperature of 450 K, which reduces the reaction rates of the 3-body $^{\cdot}OH$ recombination reactions significantly. This ~1.6 times larger $^{\cdot}OH$ lifetime in $He/Ar/H_2O$ plasma is most likely the main reason for the higher $^{\cdot}OH$ density in $He/Ar/H_2O$ compared to He/H_2O plasma. The $^{\cdot}OH$ lifetime in both He/H_2O and $He/Ar/H_2O$ plasmas is much smaller than the smallest droplet residence time in the plasma region used in this study (~4.7 ms), ensuring that the droplet is in good approximation only exposed to $^{\cdot}OH$ radicals during the droplet residence time in the plasma zone only. The steady-state $^{\cdot}OH$ density in He/H_2O plasma has previously been shown to be independent of the gas flow rate ranging from 0.5 to 1.5 slm [10].

In H_2O-containing plasmas, $H^{\cdot}$ radicals are another dominant radical species. The absolute densities of $H^{\cdot}$ radicals were determined from the calibrated TaLIF measurements as discussed in Section 2.4.2. Figure 8(b) shows the variation in the $H^{\cdot}$ densities as a function of axial position in He/H_2O and $He/Ar/H_2O$ plasmas at a total gas flow rate of 1.0 slm. The $H^{\cdot}$ densities in both He/H_2O and $He/Ar/H_2O$ plasmas reach the steady-state density of $\sim 3 \times 10^{21}$ m^{-3} within ~2 mm, followed by a fast decay in the effluent because of the short lifetime of $H^{\cdot}$ in the presence of $^{\cdot}OH$ radical, which is a highly effective quencher of $H^{\cdot}$ via three-body recombination reaction [82]. The $H^{\cdot}$ density in He/H_2O and $He/Ar/H_2O$ plasmas is almost an order of magnitude higher than the corresponding $^{\cdot}OH$ density. The high $H^{\cdot}$ density suggests a high degree of dissociation of H_2O in such plasmas (8.1% in He/H_2O and 9.5% in $He/Ar/H_2O$), conditions that favor electron impact dissociation of $^{\cdot}OH$ [83] and lead to higher densities of $H^{\cdot}$ (and possibly $O^{\cdot}$) compared to $^{\cdot}OH$. Additionally, there is much data available in literature for $O^{\cdot}$ densities in He/H_2O RF plasma [84], which allows us to conclude that the $O^{\cdot}$ density is an order of magnitude lower than the $^{\cdot}OH$ density.

The $O^{\cdot}$ density in similar RF plasmas in parallel-plate configuration has been extensively investigated previously using either O-TaLIF [85–89] or molecular beam mass spectrometry [90]. For a similar capacitively-coupled He/O_2 RF plasma with an inter-electrode gap of 1 mm, operating at atmospheric pressure and a simulated power density of 40 W/cm^3, but with an O_2 concentration of 0.6%, the $O^{\cdot}$ density from TaLIF was measured to be $\sim 2.2 \times 10^{21}$ m^{-3} [89]. Although the O_2 concentration in our work is 3 times lower, the $O^{\cdot}$ density reduced by ~42% for this drop in O_2 concentration as measured by molecular beam mass spectrometry [90]. From these literature values, we estimated for our operating conditions in the He/O_2 plasma at a similar power density of 39 W/cm^3 and an inter-electrode gap of 2 mm, an $O^{\cdot}$ density

Table 2. Electron properties and gas-phase densities of dominant radicals and metastable atoms in the glow discharges investigated in this work at the center of the discharge gap.

		Species density (m^{-3})							
Plasma	T_e (eV)	e^-	$^{\cdot}OH$	$H^{\cdot}$	$O^{\cdot}$	$O_2(a^1\Delta_g)$	O_3	$He(2^3S)$	$Ar(1s_5)$
He/O_2	3.7 ± 0.4	$9.9 \pm 1.5 \times 10^{16}$	–	–	1.55×10^{21}[a]	$2.2 \pm 0.2 \times 10^{21}$	2.2×10^{19}	–	–
He/H_2O	3.8 ± 0.4	$8.0 \pm 1.4 \times 10^{16}$	3×10^{20}	$3.4 \pm 1.2 \times 10^{21}$	$\sim 3 \times 10^{19}$[b]	$< 4 \times 10^{19}$	$< 9.8 \times 10^{18}$	$< 3.4 \times 10^{17}$	–
$He/Ar/H_2O$	3.1 ± 0.3	$1.5 \pm 0.3 \times 10^{17}$	5×10^{20}	$3.1 \pm 1.1 \times 10^{21}$	–	–	–	–	$\sim 5 \times 10^{14}$

[a] From [90]
[b] From [84]

of the order of 1.55×10^{21} m^{-3}. This is a typical value for such a plasma with variations in $O^{\cdot}$ density as a function of power and O_2 density reported in literature suggesting a maximum of 50% error in these values [89].

The $O_2(a^1\Delta_g)$ density in He + 0.2% O_2 plasma at 1 slm and 15 W is estimated to be $(2.2 \pm 0.2) \times 10^{21}$ m^{-3} from the absolute values of $O_2(a^1\Delta_g)$ and the corresponding O_3 density of $(2.2 \pm 1.5) \times 10^{19}$ m^{-3} measured in the effluent of the plasma using (1). For the same operating conditions in a He + 0.25% H_2O plasma, both the $O_2(a^1\Delta_g)$ and O_3 densities were found to be below their respective detection limits of the IR OES system (4×10^{19} m^{-3}) and the OAS system (9.8×10^{18} m^{-3}).

A summary of the electron properties and the gas-phase densities of dominant radicals and excited state atoms and molecules in the investigated plasma conditions is complied in table 2.

3.2. Droplet characterization

The residence time of the droplet in the plasma (t_{res}) is an important parameter to assess the total flux of reactive species into the droplet. Figure 9 shows the variation in the droplet residence time as a function of the total gas flow rate for both plasma off and plasma on conditions as obtained by fast imaging. The ratio of the droplet residence time between plasma off and on conditions is larger at lower flow rates and approaches unity at higher flow rates. As the droplet enters the plasma, it is accelerated due to the force induced by the electric field present in the space charge boundary at the edge of the plasma, while it is decelerated upon exiting the plasma in the direction of the gas flow (not shown). This force imparted to the droplet is dependent on the discharge power. A minimum and maximum droplet residence time of 4.7 and 13.3 ms in the He/H_2O plasma is determined for corresponding gas residence

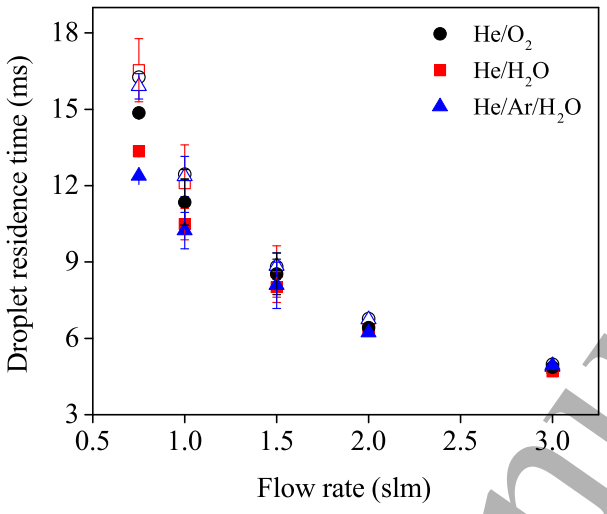

Figure 9. Droplet residence time in the plasma as a function of the total gas flow rate in He + 0.2% O_2, He + 0.2% H_2O, and He + 17% Ar + 0.2% H_2O plasmas used in this work. Open symbols represent plasma off conditions, while solid symbols represent plasma on conditions.

times of 7 and 29 ms, respectively, showing that the change in t_{res} with the gas flow rate is not a linear relationship. This deviation is due to the impact of the electric field induced acceleration of the droplet, which has a relatively larger impact on the droplet residence time for smaller gas flow rates or larger t_{res}. Even with the plasma off, the droplet residence time is lower than the gas residence time due to the effect of the gravitational force acting on the droplet.

As previously discussed in [10], a reduction in the size of the droplet was observed along the vertical axis or as a function of time during which the droplet resides in the plasma. Due to the elevated gas temperatures in the plasma, the reduction in the droplet size increased when the plasma was generated as compared to only gas flow due to evaporation. This reduction can be explained by a simple evaporation model applied to a droplet of given size in a homogeneous gas with a given temperature following these two equations expressing mass continuity and energy conservation [91]:

$$T_s = T_\infty - \frac{DML}{RK}\left(\frac{P_\infty}{T_\infty} - \frac{P_s}{T_s}\right), \text{ and} \tag{9}$$

$$\frac{d(d_p)}{dt} = \frac{4DM}{R\rho d_p}\left(\frac{P_\infty}{T_\infty} - \frac{P_s}{T_s}\right), \tag{10}$$

where T_s, T_∞, Ps, P_∞, D, M, L, R, K, ρ and d_p are the temperature at the droplet surface, the homogeneous plasma gas temperature, the water vapor pressure at the droplet surface, the homogeneous water vapor pressure, the diffusivity, the

molecular weight of water, the latent heat of vaporization, the gas constant, the thermal conductivity of the gas, the liquid density of water, and the diameter of the droplet, respectively. For He/H_2O and $He/Ar/H_2O$ plasmas, the gas temperature as a function of the droplet residence time is known from figure 5, while for He/O_2 plasma, the model is fit with the experimental data for different gas temperatures. The results for fitting of the droplet evaporation in different plasmas at a total gas flow rate of 1 slm are shown in figure 10. A maximum reduction of ∼9% and a minimum of $< 1\%$ in the droplet size were observed for He/O_2 plasma at 0.75 slm and $He/Ar/H_2O$ plasma at 3 slm, respectively, for similar plasma power of ∼14 W (not shown). The estimated gas temperature in He/O_2 plasma from the evaporation model (figure 10(a)) is similar to the measured gas temperature of ∼330 K in He plasma from the rotational temperature of OH(A) at similar plasma power [48]. In all plasma cases, the reduction in the droplet diameter decreases with increasing gas flow rates. The significantly smaller evaporation in $He/Ar/H_2O$ plasma compared to He/H_2O (figure 10(b)), despite the larger gas temperatures in $He/Ar/H_2O$ plasma, is unexpected. This is, however, also reproduced by the evaporation model. This remarkable finding is due to the lower diffusivity for water vapor and lower thermal conductivity of Ar as compared to He. The excellent agreement of the evaporation model with the experimentally measured droplet sizes in all plasma cases clearly indicates that the evaporation is due to the thermal heat transfer from the gas-phase plasma to the liquid droplet and not significantly impacted by the heating of the droplet interface due to surface recombination reactions of ions and/or radicals.

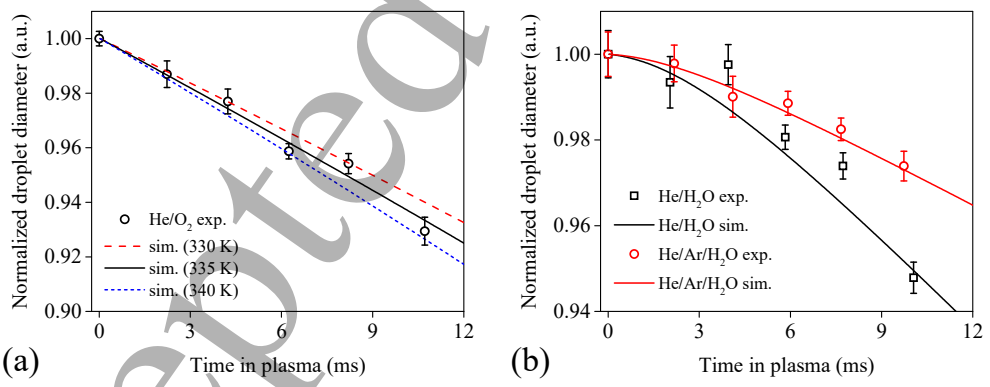

Figure 10. Normalized droplet diameters as a function of the droplet residence time in (a) He + 0.2% O_2, and (b) He + 0.2% H_2O and He + 17% Ar + 0.2% H_2O plasmas at a total gas flow rate of 1 slm and power conditions reported in table 1 for droplet diameter of 41 ± 2 μm. The reduction in the droplet size is fitted with an evaporation model as described in the text.

The number of water vapor molecules evaporating from a single droplet in the He/O_2 plasma is between 5.2×10^{13} and 2.9×10^{14}. Considering that between 6 and 19 droplets are present in the plasma region simultaneously for 3 and 0.75 slm, respectively, the total number of water vapor molecules added to the feed gas inside the plasma is between 3.2×10^{14} and 5.5×10^{15}. This leads to a possible increase in water vapor between 0.004 and 0.07%, assuming that all the water vapor is distributed evenly within the electrode cross-section of 19.1×9.5 mm, i.e. the whole plasma region. However, if we assume that the water vapor evaporating from the droplet surface is confined within a localized boundary surrounding the droplet with a cross-section of 2×2 mm, the water vapor increase could be between 0.04 and 0.61%. It has been previously shown that $^{\cdot}OH$ radical densities in good approximation scale with the root mean square of the H_2O concentration in RF discharges as used in this work [52]. Hence, an increase in water vapor concentration by a factor 2 will only increase the $^{\cdot}OH$ density by 40%. In addition, as shown later, the formate destruction is transport limited and even a significant increase in $^{\cdot}OH$ density has limited impact on the formate destruction. Nonetheless, this evaporation does not allow us to exclude an important role of $^{\cdot}OH$ radicals in formate decomposition in the He/O_2 plasma.

3.3. Formate decomposition

3.3.1. Effect of H_2O concentration Previously, it was shown that the formate in the droplet is decomposed primarily at the plasma-droplet interface by the $^{\cdot}OH$ radicals in a He + 0.2% H_2O plasma [10]. Although the $H^{\cdot}$ density is an order of magnitude higher than the $^{\cdot}OH$ density in He/H_2O plasma, the role of $H^{\cdot}$ radical in formate decomposition is negligible due to its Henry's law solubility constant that is 5 orders of magnitude smaller than that of $^{\cdot}OH$ radicals [43]. Using the Henry's law, the equilibrium concentration of $H^{\cdot}$ radical in the droplet interface is estimated to be almost 4 orders of magnitude smaller than that of the $^{\cdot}OH$ radical in He/H_2O plasma. Similarly, the $O^{\cdot}$ density in humid He RF plasma is determined to be an order of magnitude smaller than the $^{\cdot}OH$ density [84], while the electron flux to the droplet is 2 orders of magnitude smaller than the $^{\cdot}OH$ flux [10]. To study the effect of varying $^{\cdot}OH$ flux on formate decomposition in the droplet and assess the possible indications of non-$^{\cdot}OH$ induced chemistry, we varied the water concentration in the He/H_2O plasma from 0.005% to 1%. The gas-phase $^{\cdot}OH$ densities for these conditions were measured previously for similar conditions using broadband absorption spectroscopy [53]. The $^{\cdot}OH$ density increases with the water concentration in the plasma and follows a square root dependence as shown in figure 11. The $^{\cdot}OH$ density at 0.2% water concentration (3×10^{20}) m^{-3} [10] matches the values of this study within 10% difference.

The effect of the H_2O concentration (or flux) on the formate decomposition in droplets of size 43 μm is shown in figure 11. The amount of formate decomposition increases for increasing H_2O concentrations up to 0.2% H_2O and subsequently

saturates. The average formate concentration obtained from the 1D reaction-diffusion model after plasma exposure as described in Section 2.5 and [10] as a function of H_2O concentration is also plotted in figure 11 for comparison. The model has a good agreement with the measured concentrations, with exception of the 0% H_2O concentration case for which the model significantly underestimates the formate decomposition. This suggests that at the smaller $^{\cdot}OH$ densities, i.e. $n_{OH} < 10^{20}$ m^{-3} (corresponding to $< 0.05\%$ H_2O concentration), the effect of other reactive species becomes important partly because the species that are readily quenched by H_2O can become dominant, consequently changing the gas species composition. The diffusion layer near the droplet leads to a reduction in the $^{\cdot}OH$ density compared to the bulk $^{\cdot}OH$ density by a factor 11 (see Section 2.5). Using the $^{\cdot}OH$ density at the droplet interface (8×10^{18} m^{-3}) corresponding to 0.025% H_2O concentration, and the bulk n_e and T_e from the continuum radiation measurement for 0.05% H_2O (not shown), the electron flux ($\geq 3 \times 10^{12}$ s^{-1}) becomes similar to the $^{\cdot}OH$ flux (5.8×10^{12} s^{-1}) to the droplet, which shows that indeed electron/ion injection into solution and the formation of solvated electrons or $^{\cdot}OH$ and $H^{\cdot}$ radicals through charge exchange or recombination reactions might become important. Particularly at lower H_2O concentrations, local $^{\cdot}OH$ production in the vicinity of the droplet as a result of the water vapor formed by droplet evaporation might impact the $^{\cdot}OH$ flux, although it cannot readily explain

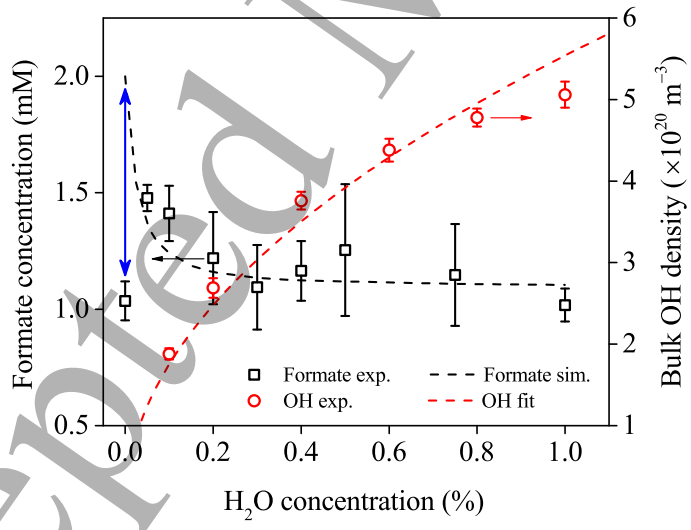

Figure 11. Average formate concentration in plasma-treated droplets as a function of water concentration in He/H_2O plasma, compared with the 1D diffusion-reaction modeling result. The discharge was operated at a total gas flow rate of 1.5 slm ($t_{res} = 8$ ms), and fixed power of 14.3 ± 0.5 W for He/H_2O plasmas and 13.6 ± 1.3 for pure He plasma. The corresponding $^{\cdot}OH$ densities are taken from [53] and follow the following relation: $n_{OH}[\text{m}^{-3}] = 5.54 \times 10^{20} \sqrt{n_{H_2O}[\%]}$.

the observed increase in decomposition. Furthermore, at low H_2O concentrations in He plasma, the ion composition could change drastically as compared to those in higher H_2O concentrations [92]. At higher H_2O concentrations, the model shows that the transport of the unreacted formate from the bulk of the droplet to the interface becomes the rate limiting step [10], rendering the formate decomposition independent of the $^{\cdot}OH$ flux, and is, thus, diffusion limited. However, at lower H_2O concentration ($< 0.2\%$), it becomes limited by the $^{\cdot}OH$ flux in the gas phase. This transport effect is illustrated in figure 12, where the spatial distribution of the concentrations of $^{\cdot}OH$ and formate near the plasma-droplet interface are shown for three different H_2O concentrations (0.025%, 0.2% and 1%) in the feed gas corresponding to the formate conversion shown in figure 11, for which no significant depletion of formate near the droplet interface is found for the lower water concentration case but an increasing depletion of formate is observed for higher $^{\cdot}OH$ fluxes.

3.3.2. Effect of droplet residence time Figure 13 shows the formate concentration in droplets with an initial diameter of 41 ± 2 μm after plasma exposure as a function of the droplet residence time in He/H_2O, He/O_2 and $He/Ar/H_2O$ plasmas. The results are all very similar for the 3 cases.

Figure 13 also shows the simulated formate decomposition in He/H_2O plasma using the 1D reaction-diffusion model to validate the effect of $^{\cdot}OH$ radical. The results

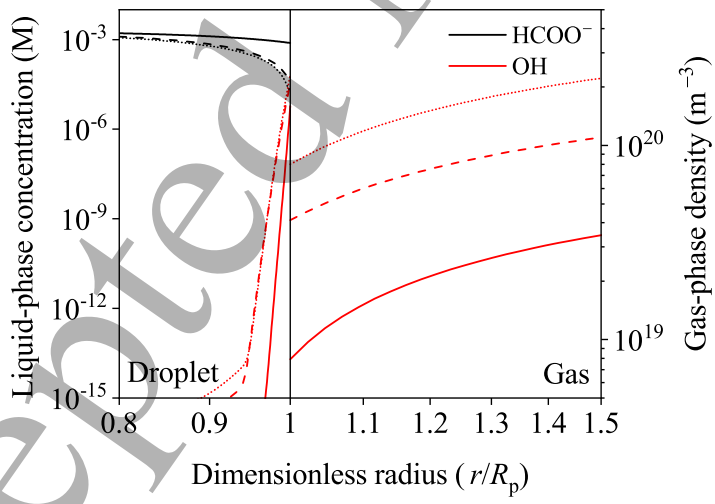

Figure 12. Radial distributions of $^{\cdot}OH$ densities near the gas–droplet interface along with the formate concentrations in the droplet for a droplet diameter of 43 μm after a plasma exposure of 8 ms corresponding to a total gas flow rate of 1.5 slm (see figure 11). The distributions are shown for H_2O concentration of 0.025% (solid line), 0.2% (dashed line) and 1.0% (dotted line) in the feed gas.

confirm the diffusion/transport limited formate conversion for $n_{OH} > 2 \times 10^{20}$ m^{-3} and the further increase in decomposition of formate with increasing plasma exposure time allowing for continued transport of the formate from the bulk of the droplet to the plasma-droplet interface.

The formate decomposition in He/O_2 plasma is remarkably similar to that of the He/H_2O plasma in spite of the reactions induced that might be dominantly induced by radicals other than $^{\cdot}$OH. The major reactive species in He/O_2 plasma are $O^{\cdot}$, $O_2(a^1\Delta_g)$ and O_3. The effect of O_3 can be neglected as it has a lower H' constant than OH [43] and a reaction rate coefficient with formate (1×10^2 M^{-1}s^{-1}) that is 7 orders of magnitude smaller than that of $^{\cdot}$OH [93], while the O_3 density in He/O_2 plasma is smaller than the OH density in He/H_2O plasma.

The investigation of the effect of $O_2(a^1\Delta_g)$ is warranted as it is known to react with organic compounds with fairly large rate coefficients of the order of $\sim 10^7 - 10^9$ M^{-1}s^{-1} [94, 95], although the reaction rate with formate is not reported. The 1D reaction-diffusion model is run with the gas-phase density of $O_2(a^1\Delta_g)$ (2.2×10^{21} m^{-3}) estimated from the measurements in the effluent. The H' and α are assumed to be the same as that of O_2. A range of $k_{O_2(a)}$ were used to fit the experimentally obtained formate decomposition. Figure 14(a) shows the results of the calculated

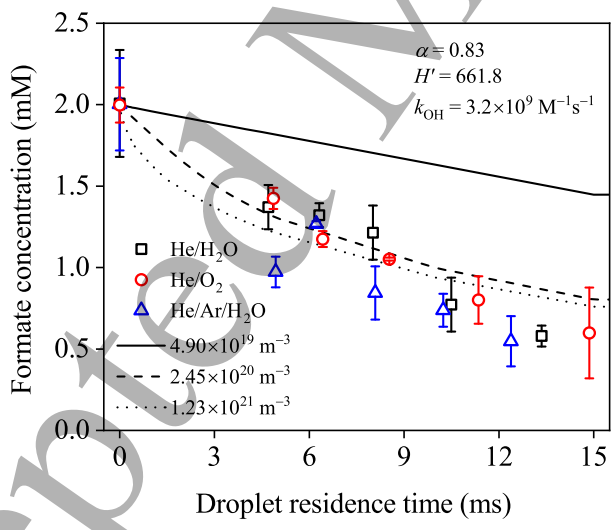

Figure 13. Average formate concentration in plasma-treated droplets as a function of droplet residence time corresponding to gas flow rates between 0.75 and 3.0 slm for an initial droplet diameter of 41 ± 2 μm in He + 0.2% H_2O, He + 0.2% O_2 and He + 17% Ar + 0.2% H_2O plasmas (open symbols). The calculated temporal evolution of average formate concentration for different values of n_{OH} fitted to the experimentally obtained results in He + 0.2% H_2O plasma is also shown (lines).

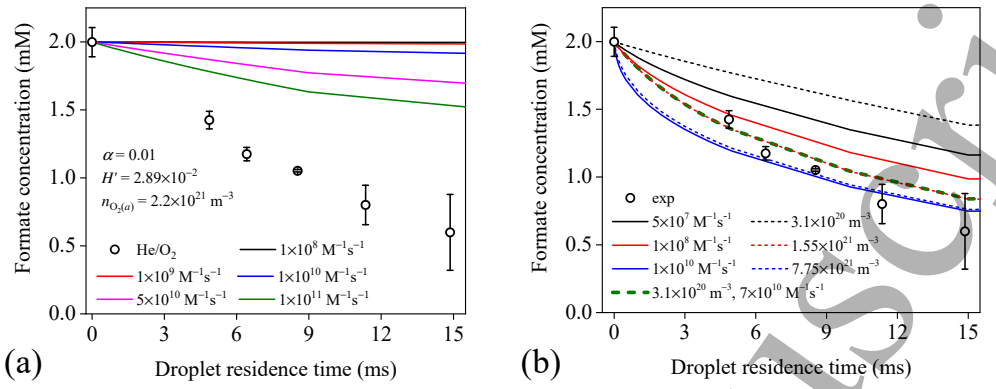

Figure 14. (a) Calculated temporal evolution of average formate concentration in liquid droplet of diameter 41 ± 2 μm for different values of $k_{O_2(a)}$ fitted to the experimentally obtained results to assess the effect of $O_2(a^1\Delta_g)$ in He + 0.2% O_2 plasma. Experimental and simulated results are presented in open symbols and solid lines, respectively. (b) Calculated average formate concentration for different values of k_O ($\alpha = 0.1$, $H' = 661.8$, $n_O = 1.55 \times 10^{21}$ m^{-3}) shown in solid lines, and n_O ($\alpha = 0.1$, $H' = 7$, $k_O = 3.2 \times 10^9$ M^{-1}s^{-1}) shown in short dashed lines fitted to the experimentally obtained results to assess the effect of O$^{\cdot}$ radical in He + 0.2% O_2 plasma. The green dashed line shows the effect of O$^{\cdot}$ on formate degradation at lower O$^{\cdot}$ density and much higher k_O value.

average formate concentration as a function of the droplet residence time for different values of $k_{O_2(a)}$. Even with an unrealistic high reaction rate coefficient, $k_{O_2(a)}$ of 1×10^{11} M^{-1}s^{-1}, the model underestimates the formate decomposition. This shows that $O_2(a^1\Delta_g)$ is not the dominant species responsible for the decomposition of formate within the investigated conditions despite being present at very large densities in the plasma. This is predominantly because of the low Henry's law constant and very short lifetime of $O_2(a^1\Delta_g)$ in liquid H_2O (4.4 μs [96]), severely limiting its transport into the droplet via solvation and/or diffusion.

This leaves us with the dominant O$^{\cdot}$ radicals as most likely species enabling (directly or indirectly) formate decomposition in the He/O_2 plasma. The O$^{\cdot}$ density in the bulk of the He/O_2 plasma is an order of magnitude higher than the $^{\cdot}$OH density in He/H_2O plasma. The recombination of O$^{\cdot}$ (effective lifetime) in background He gas can be estimated from the quenching reactions of O$^{\cdot}$ with O_2 and O_3 in the gas phase using the reaction scheme and the rate coefficient values provided in [97, 98] at a gas temperature of ~350 K. The recombination time of O$^{\cdot}$ is estimated to be in the range of 2.8–3.9 ms, depending on the reaction rate coefficients used. The diffusion time of O$^{\cdot}$ from the bulk plasma into the droplet across a sheath (h_p) of ~200 μm can be estimated by [99]

$$\tau_{\mathrm{D,O}} = \frac{\sqrt{3}R_{\mathrm{p}}h_{\mathrm{p}}}{D_{\mathrm{O-He}}}, \tag{11}$$

with $D_{\mathrm{O-He}} = 1.29 \times 10^{-4}$ m^{2}s^{-1}, the diffusion coefficient of O$^{\cdot}$ in He [89] and R_{p} the droplet radius (20.5 μm). Equation (11) yields a diffusion time of 55 μs, which is 50–70 times faster than the estimated lifetime of O$^{\cdot}$ for the investigated plasma condition. This confirms that, similar to $^{\cdot}$OH, the boundary layer acts as a sink for O$^{\cdot}$ atoms and a diffusion profile for O$^{\cdot}$ can be assumed to calculate the O$^{\cdot}$ flux (Γ_{O}) to the droplet. Using the O$^{\cdot}$ density at the droplet interface and an α value of 0.83 (assumed the same as $^{\cdot}$OH), the total O$^{\cdot}$ flux to the droplet can be estimated as:

$$\Gamma_{\mathrm{O}} \approx \frac{1}{4}\alpha G_{\mathrm{O}} v_{\mathrm{th}} \times 4\pi R_{\mathrm{p}}^2 \approx 1.1 \times 10^{15}\ \mathrm{s}^{-1}, \tag{12}$$

which is more than an order of magnitude higher than the total $^{\cdot}$OH flux to the droplet in He + 0.2% H_2O plasma (2.8×10^{13} s^{-1}), although α for O$^{\cdot}$ atom is unknown and smaller α than that of $^{\cdot}$OH might ultimately lead to smaller fluxes.

As the transport properties of O$^{\cdot}$ are not available in literature, we modeled the formate conversion in He/O_2 plasma to semi-quantitatively determine the appropriate values of α, H' and k_{O} (the rate coefficient of the reaction of O$^{\cdot}$ with formate) that provide satisfactory correspondence with the experimental measurement. In the 1D reaction-diffusion model, it was assumed that the aqueous phase concentration of O_2 at the interface in the liquid was in equilibrium with the ambient O_2 gas phase density. This is included because O$^{\cdot}$ atoms recombine with O_2 to produce O_3, which would reduce the ability of O$^{\cdot}$ to decompose formate. To assess the impact of dissolved oxygen on the formate decomposition, the model was simulated both with and without any dissolved O_2 in the liquid droplet. However, the oxidation was independent of the dissolved oxygen concentration even assuming complete O_2 saturation of the droplet. The 1D model was simulated with as base condition the values of the reaction and transport parameters the same as used for $^{\cdot}$OH. The accommodation coefficient (α) for O$^{\cdot}$ atom was varied in the range of 10^{-3} to 1 at a constant H' and k_{O} values of 661.8 and 3.2×10^9 M^{-1}s^{-1}, respectively. Although a strong effect was observed for $10^{-3} < \alpha < 5 \times 10^{-3}$, it was found to have little to no effect on formate decomposition for $\alpha > 10^{-2}$. A value of 0.1 for α is used for further modeling work. We used different values of H', ranging from 2 to that of H_2O_2 (10^6). A strong dependency was observed for $2 < H' < 100$. However, for $H' > 100$, the formate oxidation becomes independent of H'. A value of 661.8 for H' (equal to that of $^{\cdot}$OH) is, henceforth, used for assessing the impact of the reaction rates. k_{O} was varied from 5×10^7 to 1×10^{10} M^{-1}s^{-1}, which shows that a rate coefficient of at least 1×10^8 M^{-1}s^{-1} is required to predict the experimental results as shown in figure 14(b). Similarly, the gas-phase O$^{\cdot}$ density (n_{O}) was varied by a factor 5 at fixed values of transport properties ($\alpha = 0.1$, $H' = 7$, and $k_{\mathrm{O}} = 3.2 \times 10^9$ M^{-1}s^{-1}) showing the need for n_{O} in excess of 6.2×10^{21} m^{-3} if

the reaction rate of $O^{\cdot}$ with formate is the same as for $^{\cdot}OH$. These results are also shown in figure 14(b).

We can, from the above discussions, conclude that to explain the formate conversion in He/O_2 plasma, $\alpha \geq 0.003$, $H' \geq 4$ and $k_O \geq 1 \times 10^8$ $M^{-1}s^{-1}$ are required. Although the $O^{\cdot}$ radical might be the dominant species in the bulk plasma, $^{\cdot}OH$ could, in principle, be responsible for formate decomposition, since the presence of water vapor due to droplet evaporation can lead to production of $^{\cdot}OH$ from $O^{\cdot}$. The electron-induced dissociation of H_2O vapor around the droplet surface can produce $H^{\cdot}$ radicals, which can recombine with the incoming $O^{\cdot}$ radical to produce $^{\cdot}OH$. A concentration of $H^{\cdot} = 6.5 \times 10^{20}$ m^{-3} in a humid boundary layer around the droplet could convert sufficient $O^{\cdot}$ into $^{\cdot}OH$ for a typical diffusion time of 55 μs to achieve the same flux of $^{\cdot}OH$ into droplet as for the He/H_2O case. Due to evaporation, the H_2O vapor is most likely diffusing into the active plasma, which increases the $^{\cdot}OH$ density and reduces the $O^{\cdot}$ density as reported in [100]. If the $O^{\cdot}$ density reduces, the rate at which $O^{\cdot}$ reacts with formate would need to be higher in order to explain the observed formate decomposition. This case is shown in figure 14(b) in green dashed line. With a lower $O^{\cdot}$ density of 3.1×10^{20} m^{-3}, a much higher k_O of 7×10^{10} $M^{-1}s^{-1}$ would be required, which might be unlikely and $^{\cdot}OH$ radicals are more likely to be the cause of formate decomposition in this case.

A recent study showed that almost all plasma-generated $O^{\cdot}$ atoms entering the liquid phase can react with Cl^- ions in highly concentrated saline solutions [101], suggesting that both α and H' must indeed be sufficiently large. The estimated $O^{\cdot}$ density in this study is relatively high, which places the formate conversion in the transport limited regime and the impact of $^{\cdot}OH$-induced chemistry cannot be excluded. This does not allow to draw more detailed conclusions on the lower range of k_O values. In conclusion, the observed formate conversion in He/O_2 plasma could either be due to the direct impact of $O^{\cdot}$ atoms, provided the transport is sufficient, or due to $^{\cdot}OH$-induced chemistry, since addition of H_2O to He/O_2 plasma (water vapor from the droplet in this study) does not significantly impacts the $^{\cdot}OH$ density as shown in [102].

4. Conclusion

In this work, we explored the role of both OH and non-$^{\cdot}OH$ driven chemistry in the interaction between plasma and liquid micro-droplets in a controlled environment. The plasma is operated in He with different gas admixtures (Ar, O_2, humidified He) at atmospheric pressure to study the effect of $O^{\cdot}$, $H^{\cdot}$ and $^{\cdot}OH$ radicals, $O_2(a^1\Delta_g)$, O_3, and metastable He and Ar atoms on the formate decomposition in plasma-treated droplets. The plasmas are characterized using different optical diagnostic techniques to determine the electron density and temperature (OES), $^{\cdot}OH$ radical and metastable densities (BAS), $O_2(a^1\Delta_g)$ density (IR OES), O_3 density (OAS) and $H^{\cdot}$ radical

density (TaLIF). The droplet dynamics (motion and evaporation) was determined using microscopic fast imaging, from which the residence time of the droplets in the plasma could be estimated. The formate concentration was measured in the collected droplets post-plasma treatment using OAS.

The formate decomposition increased with increasing droplet residence time in the plasma in all studied cases (He/O_2, He/H_2O and $He/Ar/H_2O$). For the highest residence time of ~ 15 ms, a 70% reduction in the formate concentration was observed. A one-dimensional reaction-diffusion model was able to predict the oxidation via $^{\cdot}OH$ transport using measured gas-phase $^{\cdot}OH$ densities in He/H_2O plasma. It was further shown that at lower H_2O concentration in the plasma, the formate oxidation is gas phase $^{\cdot}OH$ flux limited. When no water vapor was added to the He feed gas, an enhanced formate decomposition was found, which might be due to the increase in the electron/ion flux to the droplet, estimated to be similar to the expected $^{\cdot}OH$ flux in this case. At higher H_2O concentrations, the formate oxidation was independent of the $^{\cdot}OH$ flux, and hence, diffusion limited. The decomposition in He/O_2 plasma was remarkably similar as for He/H_2O. The same amount of formate decomposition was achieved, although with an $O^{\cdot}$ radical density one order of magnitude larger than the $^{\cdot}OH$ density in the corresponding He/H_2O plasma. Using the reaction-diffusion model, we semi-quantitatively predicted the lower limits of the transport properties and reactions rates of $O^{\cdot}$ radical with formate ($\alpha \geq 0.003$, $H' \geq 4$ and $k_O \geq 1 \times 10^8$ $M^{-1}s^{-1}$), if $O^{\cdot}$ were solely responsible for formate decomposition in He/O_2 plasma. We showed that O_3 and $O_2(a^1\Delta_g)$ did not significantly contribute to this decomposition. However, a contribution of $^{\cdot}OH$ due to water vapor from droplet evaporation to the formate decomposition cannot be excluded.

Acknowledgments

This work was enabled by equipment and methods developed in the framework of the US Department of Energy, Office of Science, Office of Fusion Energy Sciences General Plasma Science program under Award Number DE-SC-0020232, the Army Research Office under Grant No. W911NF-20-1-0105 and the NSF grant under Award Number PHY 1903151. GN would like to thank Dr. Marien Simeni Simeni for helpful discussions on the analysis of the continuum radiation.

References

[1] Bruggeman P J, Kushner M J, Locke B R, Gardeniers J G, Graham W, Graves D B, Hofman-Caris R, Maric D, Reid J P, Ceriani E *et al.* 2016 *Plasma Sources Science and Technology* **25** 053002

[2] Foster J, Sommers B S, Gucker S N, Blankson I M and Adamovsky G 2012 *IEEE Transactions on Plasma Science* **40** 1311–1323

[3] Mariotti D, Patel J, Švrček V and Maguire P 2012 *Plasma Processes and Polymers* **9** 1074–1085

[4] Friedrich J F, Mix R, Schulze R D, Meyer-Plath A, Joshi R and Wettmarshausen S 2008 *Plasma Processes and Polymers* **5** 407–423

[5] Kong M G, Kroesen G, Morfill G, Nosenko T, Shimizu T, Van Dijk J and Zimmermann J 2009 *New Journal of Physics* **11** 115012

[6] Aboubakr H A, Gangal U, Youssef M M, Goyal S M and Bruggeman P J 2016 *Journal of Physics D: Applied Physics* **49** 204001

[7] Misra N, Schlüter O and Cullen P J 2016 *Cold plasma in food and agriculture: fundamentals and applications* (Academic Press)

[8] Sklias K, Santos Sousa J and Girard P M 2021 *Cancers* **13** 615

[9] Adamovich I, Baalrud S D, Bogaerts A, Bruggeman P, Cappelli M, Colombo V, Czarnetzki U, Ebert U, Eden J G, Favia P *et al.* 2017 *Journal of Physics D: Applied Physics* **50** 323001

[10] Oinuma G, Nayak G, Du Y and Bruggeman P J 2020 *Plasma Sources Science and Technology* **29** 095002

[11] Burlica R and Locke B R 2008 *IEEE Transactions on Industry Applications* **44** 482–489

[12] Maguire P, Rutherford D, Macias-Montero M, Mahony C, Kelsey C, Tweedie M, Pérez-Martin F, McQuaid H, Diver D and Mariotti D 2017 *Nano Letters* **17** 1336–1343

[13] Gallingani T, Abuyazid N H, Colombo V, Gherardi M and Sankaran R M 2020 *Journal of Aerosol Science* **150** 105631

[14] Toth J R, Abuyazid N H, Lacks D J, Renner J N and Sankaran R M 2020 *ACS Sustainable Chemistry & Engineering* **8** 14845–14854

[15] Merche D, Vandencasteele N and Reniers F 2012 *Thin Solid Films* **520** 4219–4236

[16] Palumbo F, Porto C L, Fracassi F and Favia P 2020 *Coatings* **10** 440

[17] Porto C L, Palumbo F, Treglia A, Camporeale G and Favia P 2019 *Japanese Journal of Applied Physics* **59** SA0801

[18] Treglia A, Palumbo F, Gristina R, Calvano C D, Cataldi T, Fracassi F and Favia P 2020 *Applied Surface Science* 146698

[19] Heyse P, Dams R, Paulussen S, Houthoofd K, Janssen K, Jacobs P A and Sels B F 2007 *Plasma Processes and Polymers* **4** 145–157

[20] Machala Z, Tarabova B, Hensel K, Spetlikova E, Sikurova L and Lukes P 2013 *Plasma Processes and Polymers* **10** 649–659

[21] Nayak G, Andrews A J, Marabella I, Aboubakr H A, Goyal S M, Olson B A, Torremorell M and Bruggeman P J 2020 *Plasma Processes and Polymers* e1900269

[22] Xia T, Kleinheksel A, Lee E, Qiao Z, Wigginton K and Clack H 2019 *Journal of Physics D: Applied Physics* **52** 255201

[23] Wu Y, Liang Y, Wei K, Li W, Yao M, Zhang J and Grinshpun S A 2015 *Applied Environmental Microbiology* **81** 996–1002

[24] Iqbal M M, Stallard C P, Dowling D P and Turner M M 2015 *Plasma Processes and Polymers* **12** 201–213

[25] Kruszelnicki J, Lietz A M and Kushner M J 2019 *Journal of Physics D: Applied Physics* **52** 355207

[26] Hassan M E, Janda M and Machala Z 2021 *Water* **13** 182

[27] Lukes P, Dolezalova E, Sisrova I and Clupek M 2014 *Plasma Sources Science and Technology* **23** 015019

[28] Hefny M M, Pattyn C, Lukes P and Benedikt J 2016 *Journal of Physics D: Applied Physics* **49** 404002

[29] Benedikt J, Hefny M M, Shaw A, Buckley B R, Iza F, Schäkermann S and Bandow J 2018 *Physical Chemistry Chemical Physics* **20** 12037–12042

[30] Gorbanev Y, O'Connell D and Chechik V 2016 *Chemistry–A European Journal* **22** 3496–3505

[31] Kondeti V S K, Gangal U, Yatom S and Bruggeman P J 2017 *Journal of Vacuum Science & Technology A: Vacuum, Surfaces, and Films* **35** 061302

[32] Rumbach P, Bartels D M, Sankaran R M and Go D B 2015 *Nature Communications* **6** 1–7

[33] Richmonds C and Sankaran R M 2008 *Applied Physics Letters* **93** 131501

[34] Jablonowski H, Sousa J S, Weltmann K D, Wende K and Reuter S 2018 *Scientific reports* **8** 1–12

[35] Locke B, Sato M, Sunka P, Hoffmann M and Chang J S 2006 *Industrial & Engineering Chemistry Research* **45** 882–905

[36] Hsieh K C, Wandell R J, Bresch S and Locke B R 2017 *Plasma Processes and Polymers* **14** 1600171

[37] Sahni M and Locke B R 2006 *Industrial & Engineering Chemistry Research* **45** 5819–5825

[38] Chen C, Liu D, Liu Z, Yang A, Chen H, Shama G and Kong M 2014 *Plasma Chemistry and Plasma Processing* **34** 403–441

[39] Buxton G V, Greenstock C L, Helman W P and Ross A B 1988 *Journal of Physical and Chemical Reference Data* **17** 513–886

[40] Taghvaei H, Kondeti V and Bruggeman P J 2019 *Plasma Chemistry and Plasma Processing* **39** 729–749

[41] Franclemont J, Fan X and Thagard S M 2015 *Journal of Physics D: Applied Physics* **48** 424004

[42] Bauer G and Graves D B 2016 *Plasma processes and polymers* **13** 1157–1178

[43] Sander R 2015 *Atmospheric Chemistry and Physics* **15** 4399–4981

[44] Zheng Y, Wang L and Bruggeman P 2020 *Journal of Vacuum Science & Technology A: Vacuum, Surfaces, and Films* **38** 063005

[45] Crapulli F, Santoro D, Sasges M and Ray A 2014 *Water Research* **64** 209–225

[46] Wende K, Williams P, Dalluge J, Van Gaens W, Aboubakr H, Bischof J, Von Woedtke T, Goyal S M, Weltmann K D, Bogaerts A *et al.* 2015 *Biointerphases* **10** 029518

[47] Kondeti V S K, Phan C Q, Wende K, Jablonowski H, Gangal U, Granick J L, Hunter R C and Bruggeman P J 2018 *Free Radical Biology and Medicine* **124** 275–287

[48] Nayak G, Sadeghi N and Bruggeman P 2019 *Plasma Sources Science and Technology* **28** 125006

[49] Nayak G, Simeni Simeni M, Rosato J, Sadeghi N and Bruggeman P 2020 *Journal of Applied Physics* **128** 243302

[50] Hofmann S, Van Gessel A, Verreycken T and Bruggeman P 2011 *Plasma Sources Science and Technology* **20** 065010

[51] Schneider C A, Rasband W S and Eliceiri K W 2012 *Nature Methods* **9** 671–675

[52] Bruggeman P, Cunge G and Sadeghi N 2012 *Plasma Sources Science and Technology* **21** 035019

[53] Du Y, Nayak G, Oinuma G, Ding Y, Peng Z and Bruggeman P J 2017 *Plasma Sources Science and Technology* **26** 095007

[54] Du Y, Nayak G, Oinuma G, Peng Z and Bruggeman P J 2017 *Journal of Physics D: Applied Physics* **50** 145201

[55] Bruggeman P J, Sadeghi N, Schram D and Linss V 2014 *Plasma Sources Science and Technology* **23** 023001

[56] Bruggeman P, Iza F, Guns P, Lauwers D, Kong M G, Gonzalvo Y A, Leys C and Schram D C 2009 *Plasma Sources Science and Technology* **19** 015016

[57] Bokor J, Freeman R, White J and Storz R 1981 *Physical Review A* **24** 612

[58] Niemi K, Schulz-Von Der Gathen V and Döbele H 2001 *Journal of Physics D: Applied Physics* **34** 2330

[59] Yatom S, Luo Y, Xiong Q and Bruggeman P J 2017 *Journal of Physics D: Applied Physics* **50** 415204

[60] Yue Y, Santosh V, Kodenti K and Bruggeman P J 2020 *Plasma Sources Science and Technology* **29** 04LT01

[61] Sousa J S and Puech V 2013 *Journal of Physics D: Applied Physics* **46** 464005

[62] Nayak G, Sousa J S and Bruggeman P J 2017 *Journal of Physics D: Applied Physics* **50** 105205

[63] Park S, Choe W, Youn Moon S and Park J 2014 *Applied Physics Letters* **104** 084103

[64] Burm K 2004 *Plasma Sources Science and Technology* **13** 387

[65] Phelps database http://www.lxcat.net retrieved on November 22, 2020

[66] Yamabe C, Buckman S and Phelps A 1983 *Physical Review A* **27** 1345

[67] Lawton S and Phelps A 1978 *The Journal of Chemical Physics* **69** 1055–1068

[68] Itikawa database http://www.lxcat.net retrieved on October 28, 2020

[69] Hayashi database http://www.lxcat.net retrieved on November 22, 2020

[70] Itikawa Y and Mason N 2005 *Journal of Physical and Chemical Reference Data* **34** 1–22

[71] Hayashi M 1987 Electron collision cross-sections for molecules determined from beam and swarm data *Swarm Studies and Inelastic Electron-Molecule Collisions* (Springer) pp 167–187

[72] Hagelaar G and Pitchford L 2005 *Plasma Sources Science and Technology* **14** 722

[73] Mai H, Shiraiwa M, Flagan R C and Seinfeld J H 2015 *Environmental Science & Technology* **49** 11485–11491

[74] Hoigné J and Bader H 1983 *Water research* **17** 185–194

[75] Bruggeman P, Verreycken T, Gonzalez M A, Walsh J L, Kong M G, Leys C and Schram D C 2010 *Journal of Physics D: Applied Physics* **43** 124005

[76] Guildner L A 1975 *Journal of research of the National Bureau of Standards. Section A, Physics and chemistry* **79** 407

[77] Van Gessel B, Brandenburg R and Bruggeman P 2013 *Applied Physics Letters* **103** 064103

[78] Patacchini L and Hutchinson I H 2009 *Physics of Plasmas* **16** 062101

[79] Vasko C, Liu D X, Van Veldhuizen E, Iza F and Bruggeman P J 2014 *Plasma Chemistry and Plasma Processing* **34** 1081–1099

[80] Verreycken T, Van Der Horst R, Sadeghi N and Bruggeman P J 2013 *Journal of Physics D: Applied Physics* **46** 464004

[81] Liu Y, Ivanov A V and Molina M J 2009 *Geophysical Research Letters* **36**

[82] Yue Y, Jiang J, Kondeti V S K and Bruggeman P J 2021 *Journal of Physics D: Applied Physics* **54** 115202

[83] Luo Y, Lietz A M, Yatom S, Kushner M J and Bruggeman P J 2018 *Journal of Physics D: Applied Physics* **52** 044003

[84] Schröter S, Wijaikhum A, Gibson A R, West A, Davies H L, Minesi N, Dedrick J, Wagenaars E, De Oliveira N, Nahon L *et al.* 2018 *Physical Chemistry Chemical Physics* **20** 24263–24286

[85] Knake N, Niemi K, Reuter S, Schulz-von der Gathen V and Winter J 2008 *Applied Physics Letters* **93** 131503

[86] Knake N, Reuter S, Niemi K, Schulz-Von Der Gathen V and Winter J 2008 *Journal of Physics D: Applied Physics* **41** 194006

[87] Reuter S, Niemi K, Schulz-Von Der Gathen V and Döbele H 2008 *Plasma Sources Science and Technology* **18** 015006

[88] Niemi K, Reuter S, Graham L, Waskoenig J and Gans T 2009 *Applied Physics Letters* **95** 151504

[89] Waskoenig J, Niemi K, Knake N, Graham L, Reuter S, Schulz-Von Der Gathen V and Gans T 2010 *Plasma Sources Science and Technology* **19** 045018

[90] Willems G, Golda J, Ellerweg D, Benedikt J, von Keudell A, Knake N and Schulz-von der Gathen V 2019 *New Journal of Physics* **21** 059501

[91] Hinds W C 1999 *Aerosol technology: properties, behavior, and measurement of airborne particles* (John Wiley & Sons)

[92] Bruggeman P, Iza F, Lauwers D and Gonzalvo Y A 2009 *Journal of Physics D: Applied Physics* **43** 012003

[93] Rumble J R 2016 NIST 40. NDRL/NIST Solution Kinetics Database: Version 3.0 Tech. rep.

[94] Young R H, Brewer D and Keller R A 1973 *Journal of the American Chemical Society* **95** 375–379

[95] Scully Jr F E and Hoigné J 1987 *Chemosphere* **16** 681–694

[96] Rodgers M A and Snowden P T 1982 *Journal of the American Chemical Society* **104** 5541–5543

[97] Jeong J Y, Park J, Henins I, Babayan S E, Tu V J, Selwyn G S, Ding G and Hicks R F 2000 *The Journal of Physical Chemistry A* **104** 8027–8032

[98] Ellerweg D, Von Keudell A and Benedikt J 2012 *Plasma Sources Science and Technology* **21** 034019

[99] Alvarez N J, Walker L M and Anna S L 2010 *Physical Review E* **82** 011604

[100] McKay K, Liu D, Rong M, Iza F and Kong M 2012 *Journal of Physics D: Applied Physics* **45** 172001

[101] Jirásek V and Lukeš P 2020 *Journal of Physics D: Applied Physics* **53** 505206

[102] Brisset A, Gibson A R, Schröter S, Niemi K, Booth J P, Gans T, O'Connell D and Wagenaars E 2021 *Journal of Physics D: Applied Physics* **54** 285201